A top-down assessment using OMI NO$_2$ suggests an underestimate in the NOx emissions inventory in Seoul, South Korea during KORUS-AQ

Daniel L. Goldberg[*,1,2], Pablo E. Saide[3], Lok N. Lamsal[4,5], Benjamin de Foy[6], Zifeng Lu[1,2], Jung-Hun Woo[7], Younha Kim[7], Jinseok Kim[7], Meng Gao[8], Gregory Carmichael[9], and David G. Streets[1,2]

[1]Energy Systems Division, Argonne National Laboratory, Argonne, IL 60439 USA
[2]Consortium for Advanced Science and Engineering, University of Chicago, Chicago, IL 60637, USA
[3]Department of Atmospheric and Oceanic Sciences, Institute of the Environment and Sustainability, University of California – Los Angeles, Los Angeles, CA 90095, USA
[4]Goddard Earth Sciences Technology and Research, Universities Space Research Association, Columbia, MD 21046, USA
[5]NASA Goddard Space Flight Center, Code 614, Greenbelt, MD 20771, USA
[6]Department of Earth and Atmospheric Sciences, Saint Louis University, St. Louis, MO 63108, USA
[7]Konkuk University, 05029 Seoul, South Korea
[8]School of Engineering and Applied Sciences, Harvard University, Cambridge, MA 02138, USA
[9]Department of Chemical and Biochemical Engineering, University of Iowa, Iowa City, IA 52242, USA
Correspondence to: Daniel L. Goldberg (dgoldberg@anl.gov)

Abstract. In this work, we investigate the NO$_x$ emissions inventory in Seoul, South Korea using a regional Ozone Monitoring Instrument (OMI) NO$_2$ product derived from the standard NASA product. We first develop a regional OMI NO$_2$ product by re-calculating the air mass factors using a high-resolution (4 × 4 km^2) WRF-Chem model simulation, which better captures the NO$_2$ profile shapes in urban regions. We then apply a model-derived spatial averaging kernel to further downscale the retrieval and account for the sub-pixel variability. These two modifications yield OMI NO$_2$ values in the regional product that are 1.37 larger in the Seoul metropolitan region and >2 times larger near substantial point sources. These two modifications also yield an OMI NO$_2$ product that is in better agreement with the Pandora NO$_2$ spectrometer measurements acquired during the Korea U.S.-Air Quality (KORUS-AQ) field campaign. NO$_x$ emissions are then derived for the Seoul metropolitan area during the KORUS-AQ field campaign using a top-down approach with the standard and regional NASA OMI NO$_2$ products. We first apply the top-down approach to a model simulation to ensure that the method is appropriate: the WRF-Chem simulation utilizing the bottom-up emission inventory yields a NO$_x$ emission rate of 227 ± 94 kton/yr, while the bottom-up inventory itself yields a NO$_x$ emission rate of 198 kton/yr. Using the top-down approach on the regional OMI NO$_2$ product, we derive the NO$_x$ emissions rate from Seoul to be 484 ± 201 kton/yr, and a 353 ± 146 kton/yr NO$_x$ emissions rate using the standard NASA OMI NO$_2$ product. This suggests an underestimate of 53% and 36% using the regional and standard NASA OMI NO$_2$ products respectively. To supplement this finding, we compare the NO$_2$ and NO$_y$ simulated by WRF-Chem to observations of the same quantity acquired by aircraft and find a model underestimate. When NO$_x$ emissions in the WRF-Chem model are increased by a factor of 2.13 in the Seoul metropolitan area, there is better agreement with KORUS-AQ aircraft observations and the re-calculated OMI NO$_2$ tropospheric columns. Finally, we show that by using a WRF-Chem simulation with an updated emissions inventory to re-calculate the AMF, there are small differences (~8%) in OMI NO$_2$ compared to using the original WRF-Chem simulation to derive the AMF. This suggests that changes in model resolution have a larger effect on the AMF calculation than modifications to the Korean

1

emissions inventory. Although the current work is focused on South Korea using OMI, the methodology developed in this work can be applied to other world regions using TROPOMI and future satellite datasets (e.g., GEMS and TEMPO) to produce high-quality region-specific top-down NO_x emission estimates.

1 Introduction

Nitrogen oxides ($NO_x \equiv NO + NO_2$) are a group of reactive trace gases that are toxic to human health and can transform in the atmosphere into other noxious chemical species. In the presence of abundant volatile organic compounds and strong sunlight, NOx can participate in a series of chemical reactions to accelerate the production of O_3, another toxic air pollutant with a longer atmospheric lifetime. NO_x can also transform into particulate nitrate, a component of fine particulate matter ($PM_{2.5}$), an additional health hazard. When fully oxidized in the atmosphere, NO_x transforms into HNO_3, a key contributor to acid rain. There are some biogenic emissions of NO_x (e.g., lightning), but the majority of the NO_x emissions are from anthropogenic sources (van Vuuren et al., 2011).

There is a rich legacy of NO_2 measurements by remote sensing instruments (Burrows et al., 1999). One of these instruments is the Dutch-Finnish Ozone Monitoring Instrument (OMI), which measures the absorption of solar backscatter in the UV-visible spectral range. NO_2 can be observed from space because it has strong absorption features within the $400 - 465$ nm wavelength region (Vandaele et al., 1998). By comparing observed spectra with a reference spectrum, the amount of NO_2 in the atmosphere between the instrument in low-earth orbit and the surface can be derived; this technique is called differential optical absorption spectroscopy (DOAS) (Platt, 1994).

Tropospheric NO_2 column contents from OMI have been used to estimate NO_x emissions from various areas around the globe (Streets et al., 2013; Miyazaki et al., 2017) including North America (Boersma et al., 2008; Lu et al., 2015), Asia (Zhang et al., 2008; Han et al, 2015; Kuhlmann et al., 2015; Liu et al., 2017), the Middle East (Beirle et al., 2011), and Europe (Huijnen et al., 2010; Curier et al., 2014). It has also been used to produce and validate NO_x emission estimates from sectors such as soil (Hudman et al., 2010; Vinken et al., 2014a; Rasool et al., 2016), lightning (Allen et al., 2012; Liaskos et al., 2015; Pickering et al., 2016; Nault et al., 2017), power plants (de Foy et al., 2015), aircraft (Pujadas et al., 2011), marine vessels (Vinken et al., 2014b; Boersma et al., 2015), and urban centers (Lu et al., 2015; Canty et al., 2015; Souri et al., 2016).

With a pixel resolution varying from 13×24 km^2 to 26×128 km^2, the OMI sensor was developed for global to regional scale studies rather than for individual urban areas. Even at the highest spatial resolution of 13×24 km^2, the sensor has difficulty observing the fine structure of NO_2 plumes at or near the surface (e.g., highways, power plants, factories, etc.) (Chen et al., 2009; Ma et al., 2013; Flynn et al., 2014), which are often less than 10 km in width (Heue et al., 2008). This can lead to a spatial averaging of pollution (Hilboll et al., 2013). A temporary remedy, until higher spatial resolution satellite instruments are operational, is to use a regional air quality simulation to estimate the sub-pixel variability of OMI pixels. Kim et al. (2016) utilize the spatial variability in a regional air quality model to spatially downscale OMI NO_2 measurements using a spatial averaging kernel. The spatial averaging kernel technique has shown to increase the OMI NO_2 signal within urban areas, which is in better agreement with observations in these regions (Goldberg et al., 2017).

Furthermore, the air mass factor and surface reflectance used in obtaining the global OMI NO_2 retrievals are at a coarse spatial resolution (Lorente et al. 2017; Kleipool et al., 2008). While appropriate for a global operational

retrieval, this is known to cause an underestimate in the OMI NO_2 signal in urban regions (Russell et al., 2011). The air mass factors in operational OMI NO_2 are calculated using NO_2 profile shapes that are provided at a $1.25° \times 1°$ spatial resolution in the NASA product (Krotkov et al. 2017) and $2° \times 3°$ spatial resolution in the DOMINO product (Boersma et al., 2011). Developers of the NASA product provide scattering weights and additional auxiliary information so that users can develop their own tropospheric vertical column product a posteriori (Lamsal et al. 2015). Several users have re-calculated the air mass factor using a regional air quality model (Russell et al., 2011; Kuhlmann et al, 2015; Lin et al., 2015; Goldberg et al., 2017), which can better capture the NO_2 profile shapes in urban regions. Other techniques to improve the air mass factor involve correcting for the surface pressure in mountainous terrain (Zhou et al., 2009) and accounting for small-scale heterogeneities in surface reflectance (Zhou et al., 2010; Vasilkov et al., 2017). These a posteriori products have better agreement with ground-based spectrometers measuring tropospheric vertical column contents (Goldberg et al., 2017). When available, observations from aircraft can constrain the NO_2 profile shapes used in the air mass factor calculation (Goldberg et al., 2017).

In this paper, we apply both techniques (the spatial averaging kernel and an air mass factor adjustment) to develop a regional OMI NO_2 product for South Korea. We then use the regional product with only the air mass factor adjustment to derive NO_x emission estimates for the Seoul metropolitan area using an exponentially modified Gaussian (EMG) function (Beirle et al., 2011; Valin et al., 2013; de Foy et al., 2014; Lu et al., 2015); the methodology is described in-depth in Section 2.5.

2 Methods

2.1 OMI NO_2

OMI has been operational on NASA's Earth Observing System (EOS) Aura satellite since October 2004 (Levelt et al., 2006). The satellite follows a sun-synchronous, low-earth (705 km) orbit with an equator overpass time of approximately 13:45 local time. OMI measures total column amounts in a 2600 km swath divided into 60 unequal area "field-of-views", or pixels. At nadir (center of the swath), pixel size is 13×24 km^2, but at the swath edges, pixels can be as large as 26×128 km^2. In a single orbit, OMI measures approximately 1650 swaths and achieves daily global coverage over 14 – 15 orbits (99 minutes per orbit). Since June 2007, there has been a partial blockage of the detector's full field of view, which has limited the number of valid measurements by blocking consistent rows of data; this is known in the community as the row anomaly (Dobber et al., 2008): http://projects.knmi.nl/omi/research/product/rowanomaly-background.php.

OMI measures radiance data between the instrument's detector and the Earth's surface. Comparison of these measurements with a reference spectrum (i.e., DOAS technique), enables the calculation of the total slant column density (SCD), which represents an integrated trace gas abundance from the sun to the surface and back to the instrument's detector, passing through the atmosphere twice. For tropospheric air quality studies, vertical column density (VCD) data are more useful. This is done by subtracting the stratospheric slant column from the total

(tropospheric + stratospheric) slant column and dividing by the tropospheric air mass factor (AMF), which is defined as the ratio of the SCD to the VCD, as shown in Eq. (1):

$$VCD_{trop} = \frac{SCD_{total} - SCD_{strat}}{AMF_{trop}} \qquad , \text{ where } AMF_{trop} = \frac{SCD_{trop}}{VCD_{trop}} \qquad (1)$$

The tropospheric AMF has been derived to be a function of the optical atmospheric/surface properties (viewing and solar angles, surface reflectivity, cloud radiance fraction, and cloud height) and a priori profile shape (Palmer et al., 2001; Martin et al., 2002) and can be calculated as follows (Lamsal et al., 2014) in Eq. (2):

$$AMF_{trop} = \frac{\sum_{n=surface}^{tropopause} SW_n \times x_n}{\sum_{n=surface}^{tropopause} x_n} \qquad (2)$$

where x is the partial column. The optical atmospheric/surface properties in the NASA retrieval are characterized by the scattering weight and are calculated by a forward radiative transfer model (TOMRAD), which are output as a look-up table. The scattering weights are then adjusted real-time depending on observed viewing angles, surface albedo, cloud radiance fraction, and cloud pressure.

For this study, we follow previous studies (e.g., Palmer et al., 2001, Martin et al., 2002, Boersma et al., 2011, Bucsela et al., 2013) and assume that scattering weights and trace gas profile shapes are independent. The a priori trace gas profile shapes (x_a) must be provided by a model simulation. In an operational setting, NASA uses a monthly-averaged and year-specific Global Model Initiative (GMI) global simulation with a spatial resolution of 1.25° lon × 1° lat (~110 km × 110 km in the mid-latitudes) to provide the a priori profile shapes.

We derive tropospheric VCDs using a priori NO_2 profile shapes from a regional WRF-Chem simulation. A full description of this methodology can be found in Goldberg et al. (2017); it is also described in brief in section 2.1.1. We filter the Level 2 OMI NO_2 data to ensure only valid pixels are used. Daily pixels with solar zenith angles ≥ 80°, cloud radiance fractions ≥ 0.5, or surface albedo ≥ 0.3 are removed as well as the five largest pixels at the swath edges (i.e., pixel numbers 1 – 5 and 56 – 60). Finally, we remove any pixel flagged by NASA including pixels with NaN values, 'XTrackQualityFlags' ≠ 0 or 255 (RA flag), or 'VcdQualityFlags' > 0 and least significant bit ≠ 0 (ground pixel flag).

2.1.1 OMI-WRF-Chem NO_2

We modify the air mass factor in the OMI NO_2 retrieval based on the vertical profiles from a high spatial (4×4 km^2) resolution WRF-Chem simulation. The vertical profiles are scaled based on a comparison with in situ aircraft observations; this accounts for any consistent biases in the model simulation. For example, if the aircraft observations show that mean NO_2 concentrations between 0 - 500 m are low by 50%, then we scale the modeled NO_2 in this altitude bin by this same amount. To re-calculate the air mass factor for each OMI pixel, we first compute sub-pixel air mass factors for each WRF-Chem model grid cell, using the same method as outlined in Goldberg et al. (2017). The sub-

pixel air mass factor for each WRF-Chem grid cell is a function of the modelled NO_2 profile shape and the scattering weight calculated by a radiative transfer model. We then average all sub-pixel air mass factors within an OMI pixel (usually 10-100) to generate a single tropospheric air mass factor for each individual OMI pixel. This new air mass factor is used to convert the total slant column into a total vertical column using Equation 1. Model outputs were sampled at the local time of OMI overpass. For May 2016, we used daily NO_2 profiles and terrain pressures (e.g., (Zhou et al., 2009, Laughner et al., 2016)) to re-calculate the AMF. For other months and years, we used May 2016 monthly mean values of NO_2 and tropopause pressures for the a priori profiles, which are used in the calculation of the AMF.

Once the tropospheric vertical column of each OMI pixel was re-calculated, the product was oversampled (de Foy et al., 2009; Russell et al., 2010) for April – June over a 3-year period (2015-2017; 9 months total). During this timeframe, there are approximately 9 valid OMI NO_2 pixels per month over any given location on the Korean peninsula. In the top-down emissions derivation, we use all nine-months of OMI data for the analysis.

2.2 NO_2 observations during KORUS-AQ

We use in situ NO_2 observations from the KORUS-AQ field campaign to test the regional satellite product. KORUS-AQ was a joint Korea-US field experiment designed to better understand the trace gas and aerosol composition above the Korean peninsula using aircrafts, ground station networks, and satellites. The campaign took place between May 1, 2016 and June 15, 2016 and measurements were primarily focused in the Seoul Metropolitan Area. In this paper, we utilize data acquired by the ground-based Pandora spectrometer network, the thermally dissociated laser-induced fluorescence NO_2 instrument on DC-8 aircraft, and the chemiluminescence NO_y instrument on the DC-8 aircraft (NO_y = $NO + NO_2 + HNO_3 + 2 \times N_2O_5$ + peroxy nitrates + alkyl nitrates + …). KORUS-AQ observations were retrieved from the online data archive: http://www-air.larc.nasa.gov/cgi-bin/ArcView/korusaq. A further description of this field campaign can be found in the KORUS-AQ White Paper (https://espo.nasa.gov/korus-aq/content/KORUS-AQ_Science_Overview_0).

2.2.1 Pandora NO_2 data

Measurements of total column NO_2 from the Pandora instrument (Herman et al., 2009; Herman et al., 2018) are used to evaluate the OMI NO_2 satellite products. The Pandora instrument is a stationary, ground-based, sun-tracking spectrometer, which measures direct sunlight in the UV-Visible spectral range (280-525 nm) with a sampling period of 90 seconds. The Pandora spectrometer measures total column NO_2 using a DOAS technique similar to OMI. A distinct advantage of the Pandora instrument is that it does not require complex assumptions for converting slant columns into vertical columns, compared to zenith sky measurements (e.g., MAX-DOAS).

Valid OMI NO_2 pixels are matched spatially and temporally to Pandora total column NO_2 observations. To smooth the data and eliminate brief small-scale plumes that would be undetectable by a satellite, we average the Pandora observations over a two hour period (± one hour of the overpass time) before matching to the OMI NO_2 data (Goldberg

et al., 2017). During May 2016, there were seven Pandora NO_2 spectrometers operating during the experiment (five instruments were situated within the Seoul metropolitan area and their locations are shown in Figure 5); this corresponded to fifty instances in which valid Pandora NO_2 observations matched valid OMI NO_2 column data.

2.2.2 DC-8 aircraft data

5   We compare the model simulation to in situ NO_2 data gathered by the UC-Berkeley Cohen group (Thornton et al., 2000; Day et al, 2002) on the DC-8 aircraft. The instrument quantifies NO_2 via laser-induced fluorescence at 585 nm. This instrument does not have the same positive bias as chemiluminescence NO_2 detectors, so there is no need to modify NO_2 concentrations by applying an empirical equation (e.g., Lamsal et al., 2008). We also compare the model simulation to chemiluminescence NO_y data gathered by the NCAR Weinheimer group (Ridley et al., 2004)

10   We utilize one-minute averaged DC-8 data from all fourteen flights during May – June 2016. A typical flight path included several low-altitude spirals over the Seoul Metropolitan Area and a long-distance transect over the Korean peninsula or the Yellow Sea. One-minute averaged data is already pre-generated in the data archive. Hourly output from the model simulation is spatially and temporally matched to the observations. We then bin the data into different altitude ranges for our comparison.

15   **2.3 WRF-Chem model simulation**

For the high-resolution OMI NO_2 product, we use a regional simulation of the Weather Research & Forecasting (Skamarock et al., 2008) coupled to Chemistry (WRF-Chem) (Grell et al., 2005) in forecast mode prepared for flight planning during the KORUS-AQ field campaign. The forecast simulations were performed daily and used National Centers for Environmental Prediction Global Forecast System (https://rda.ucar.edu/datasets/ds084.6/) meteorological

20   initial and boundary conditions from the 06 UTC cycle. Initial conditions for aerosols and gases were obtained from the previous forecasting cycle, while Copernicus Atmosphere Monitoring Service (Inness et al., 2015) forecasts were used as boundary conditions. WRF-Chem was configured with two domains, with 20 km and 4 km grid-spacing. The 20 km domain included the major sources for trans-boundary pollution impacting the Korean peninsula (deserts in China and Mongolia, wild-fires in Siberia and anthropogenic sources from China). The 4 km domain provided a high-

25   resolution simulation where detailed local sources could be modeled and where the KORUS-AQ flight tracks were contained. The inner domain was started 18 hours after the outer domain, and was simulated for 33 hours (00UTC from day 1 to 9 UTC of day 2 of the forecast); output was saved hourly. The last 24 hours of each inner domain daily forecast over the course of KORUS-AQ were selected to allow spin-up from the outer domain and were used in the analysis presented here.

30   WRF-Chem was configured with 4 bin MOSAIC aerosols (Zaveri et al., 2008), a reduced hydrocarbon trace gas chemical mechanism (Pfister et al., 2014) including simplified secondary organic aerosol formation (Hodzic and Jimenez, 2011), and with capabilities to assimilate satellite aerosol optical depth both from low-earth orbiting and geostationary satellites (Saide et al., 2013, 2014).

2.4 Emission Inventory

The WRF-Chem simulation was driven by emissions developed by Konkuk University. Monthly emissions for South Korea were developed using the projected 2015 Korean national emissions inventory, Clean Air Policy Support System (CAPSS) provided by the National Institute of Environmental Research of Korea and with enhancements by Konkuk University, which primarily include the addition of new power plants. The projected CAPSS 2015 emissions were estimated based on CAPSS 2012 and 3-year growth factors. Since the base year of the inventory is 2012, observed emissions from the post-2013 Large Point Source inventory were not included. Emissions from China and North Korea were taken from the Comprehensive Regional Emissions for Atmospheric Transport Experiments (CREATE) v3.0 emissions inventory. In order to project the year 2010 emissions to 2015, the latest energy statistics from the International Energy Agency (http://www.iea.org/weo2017/) and the China Statistical Yearbook 2016 (http://www.stats.gov.cn/tjsj/ndsj/2016/indexeh.htm) were used to update the growth of fuel activities. In addition, the new emissions control policies in China, which were compiled by the International Institute for Applied Systems Analysis, were applied to consider efficiencies of emissions control (van der A et al., 2017).

Emissions were first processed to the monthly time-scale at a spatial resolution of 3 km in South Korea and 0.1° for the rest of Asia using SMOKE-Asia (Woo et al., 2012). Information from GIS, such as population, road network, and land cover, were applied to generate gridded emissions from the region-based (17 metropolitan and provincial boundaries of South Korea) emissions. The GIS-based population and regional boundary data compiled by the Ministry of Interior and Safety (http://www.mois.go.kr/frt/sub/a05/totStat/), and land cover data compiled by the Ministry of Environment (https://egis.me.go.kr/) were used to generate population and land cover based spatial surrogates. The Road and Railroad network data compiled by The Korea Transport Institute were used to generate spatial surrogates for onroad and nonroad emissions (https://www.koti.re.kr/). The emissions were downscaled temporally from monthly to hourly and spatially re-allocated to 4 km over South Korea and 20 km over the rest of East Asia using the University of Iowa emission pre-processor (EPRES).

Biogenic emissions are included using the on-line Model of Emissions of Gases and Aerosols from Nature (MEGAN) model version 2; there are no NO_x emissions from MEGAN. For this simulation, the lightning NO_x parameterization was turned off. For wildfires we used the Quick Fire Emissions Dataset (QFED2), but there were only isolated, small fires in South Korea during this timeframe.

2.5 Exponentially Modified Gaussian Fitting Method

An exponentially modified Gaussian (EMG) function is fit to a collection of NO_2 plumes observed from OMI in order to determine the NO_2 burden and lifetime from the Seoul metropolitan area. The original methodology, proposed by Beirle et al. (2011), involves the fitting of OMI NO_2 line densities to an EMG function. OMI NO_2 line densities are the integral of OMI NO_2 retrieval perpendicular to the path of the plume; the units are mass per distance. We define integration length scale as the across plume width. The across plume width is dependent on the NO_2 plume size and

can vary between 10 km (for small point sources) to 240 km (for large urban areas). Visual inspection of the rotated oversampled OMI NO_2 plumes is the best way to determine the spatial extent of the emission sources (Lu et al. 2015).

The EMG model is expressed as Equation (3):

$$OMI\ NO_2\ Line\ Density\ = \alpha \left[\frac{1}{x_o} exp\left(\frac{\mu}{x_o} + \frac{\sigma^2}{2x_o^2} - \frac{x}{x_o}\right) \Phi\left(\frac{x-\mu}{\sigma} - \frac{\sigma}{x_o}\right)\right] + \beta \qquad (3)$$

where α is the total number of NO_2 molecules observed near the hotspot, excluding the effect of background NO_2, β; x_o is the e-folding distance downwind, representing the length scale of the NO_2 decay; μ is the location of the apparent source relative to the city center; σ is the standard deviation of the Gaussian function, representing the Gaussian smoothing length scale; Φ is the cumulative distribution function. Using the 'curvefit' function in IDL, we determine the five unknown parameters: α, x_o, σ, μ, β based on the independent (distance; x) and dependent (OMI NO_2 line density) variables.

Using the mean zonal wind speed, w, of the NO_2 line density domain, the mean effective NO_2 lifetime $\tau_{effective}$ and the mean NOx emissions can be calculated from the fitted parameters x_o and α. The wind speed and direction are obtained from the ERA-Interim re-analysis project (Dee et al., 2011), instead of the WRF simulation because the WRF simulation is a forecast. We use the averaged wind fields of the bottom eight levels of the re-analysis (i.e., from the surface to ~500 m). Only days in which the wind speeds are > 3 m/s are included in this analysis, because NO_2 decay under this condition is dominated by chemical removal, not variability in the winds (de Foy et al., 2014). The factor of 1.33 is the mean column-averaged NO_x / NO_2 ratio in the WRF-Chem model simulation for the Seoul metropolitan area during the mid-afternoon. The NO_x / NO_2 ratio is time-dependent, spatially varying and is primarily a function of the localized $j(NO_2)$ and O_3 concentration.

$$NO_x\ Emissions = 1.33 \left(\frac{\alpha}{\tau_{effective}}\right), \text{where } \tau_{effective} = \frac{x_o}{w} \qquad (4)$$

The NO_2 plume concentration is a function of the emission source strength, wind speed, and wind direction. Originally, the method separated all NO_2 plumes by wind direction, and fit an EMG function to NO_2 in eight wind directions (Beirle et al., 2011; Ialongo et al., 2014; Liu et al., 2016). Newer methodologies rotate the plumes so that all plumes are in the same direction (Valin et al., 2013; de Foy et al., 2014; Lu et al., 2015). This process increases the signal-to-noise ratio and generates a more robust fit. In this work, we filter OMI NO_2 data and rotate the NO_2 plumes and as described in Lu et al. (2015), so that all plumes are decaying in the same direction. We rotate the retrieval based on the re-analyzed 0-500 m wind speed direction from the ERA-Interim. In doing so, we develop a re-gridded satellite product in an x-y coordinate system, in which the urban plume is aligned along the x-axis. Following de Foy et al. (2014) and Lu et al. (2015), we only use days in which the ERA-Interim wind speeds are > 3 m/s because there is more direct plume transport and less plume meandering on days with stronger winds; this yields more robust NO_x emission estimates. We fit an EMG function to the line density as function of the horizontal distance. This yields a single value at each point along the x-direction.

3 Results

In this section, we describe the regional high-resolution satellite product and our validation efforts. All OMI NO$_2$ results presented here are vertical column densities. First, we show a continental snapshot of OMI NO$_2$ (OMI-Standard) over East Asia using the standard NASA product. Then, we show a regional NASA OMI NO$_2$ satellite
5   product (OMI-Regional) using AMFs generated from the WRF-Chem a priori NO$_2$ profiles. We compare the OMI-Regional product with NO$_2$ VCDs from the original WRF-Chem simulation. We evaluate the OMI-Regional product by comparing to KORUS-AQ observations. Finally, we use the OMI-Standard and OMI-Regional products to estimate NO$_x$ emissions from the Seoul metropolitan area.

3.1 OMI NO$_2$ in East Asia

10   Oversampled OMI NO$_2$ for May – September 2015 – 2017 (15 months total) in East Asia and the 4 km WRF-Chem model domain are shown in Figure 1. The OMI NO$_2$ signals in East Asia over major metropolitan areas are 3 to 5 times larger than over similarly sized cities in the US (Krotkov et al., 2016). This is in despite of recent NO$_x$ reductions in China since 2011 (de Foy et al., 2016; Souri et al., 2017; Zheng et al., 2018). OMI has observed a recent decrease in the NO$_2$ burden in the immediate Seoul, South Korea metropolitan area, but an increase in areas just outside the
15   city center (Duncan et al., 2016). Oversampled values greater than 8×10^{15} molecules per cm^2 are still consistently seen in East Asia, while they are non-existent in the US during the warm season.

3.2 Calculation of new OMI tropospheric column NO$_2$

In Figure 2, we plot the OMI-Standard and OMI-Regional products over South Korea. The top center panel shows a regional product in which only the air mass factor correction is applied (AMF). The bottom center panel shows a
20   regional product in which the air mass factor correction and spatial averaging kernel are applied (AMF+SK). The regional product yields larger OMI NO$_2$ values throughout the majority of the Korean peninsula. Areas near major cities (e.g. Seoul), power plants, steel mills, and cement kilns have OMI NO$_2$ values that are >1.25 times larger in the regional AMF product and >2 times larger in the regional AMF+SK product. There are two reasons for the larger OMI NO$_2$ signals: the air mass factors in polluted regions are now smaller (Russell et al., 2011; Goldberg et al., 2017)
25   and the spatial weighting kernel allocates a large portion of the OMI NO$_2$ signal into a smaller region (Kim et al., 2016).

3.3 OMI-Regional vs. WRF-Chem

We now compare the OMI-Regional product to tropospheric vertical columns from the WRF-Chem model simulation directly. In Figure 3, we compare the regional satellite product (AMF+SK) to the WRF-Chem simulation over the
30   Korean peninsula. In most areas, the modeled tropospheric column NO$_2$ is of smaller magnitude than inferred by the satellite. In the area within 40 km of the Seoul city center, modeled tropospheric vertical columns are 44% smaller than observed tropospheric vertical column in the regional AMF+SK product. We posit four reasons as to why the model simulation calculates columns that are consistently smaller. First, WRF-Chem uses a reduced hydrocarbon

gas-phase chemical mechanism. This fast-calculating mechanism implemented in WRF-Chem for regional climate assessments (Pfister et al., 2014) and used during KORUS-AQ for forecasting does not quickly recycle alkyl nitrates back to NO_2; this will cause NO_2 to be too low. While an underestimate of the chemical conversion to NO_2 in WRF-Chem is a contributor to the underestimate, it likely does not account for the entire discrepancy; Canty et al., (2015) suggests that by shortening the lifetime of alkyl nitrates in the chemical mechanism, NO_2 will increase by roughly 3% in urban areas and 18% in rural areas. Second, an underestimate in VOC emissions would have an impact on peroxyacyl and alkyl nitrate formation, and should enhance the effective NO_x lifetime (Romer et al., 2016). Third, the temporal allocation of NO_x emissions in this WRF-Chem simulation is such that the early afternoon rate (between 12:00 – 14:00 local time) is approximately equal to 24-hour averaged rate (Figure 4). For comparison, using SMOKE in the eastern US yields an early afternoon emission rate that is 1.35 larger than the 24-hour averaged emission rate. Lastly, the remaining difference will likely be due to an underestimate in the emissions inventory.

3.4 Comparing WRF-Chem to Aircraft Measurements

When comparing the model simulation to in situ observations from the UC-Berkeley NO_2 instrument aboard the aircraft, we find that NO_2 concentrations are substantially larger than the model when spatially and temporally co-located in the immediate Seoul metropolitan area (Figure 5). The comparison isolates the NO_2 within the lowermost boundary layer as the primary contributor to the tropospheric column underestimate. When comparing aircraft NO_2 to modeled NO_2 in other areas of the Korean peninsula, the underestimate is smaller.

When comparing the model simulation of NO_y to observations of the same quantity observed from the aircraft, we find a similarly large underestimate. NO_y observed on the aircraft is roughly a factor of two larger at all altitudes below 2 km. This suggests that errors in NO_2 recycling ($NO_2 \leftrightarrow NO_y$) are not the main cause of the NO_2 discrepancies seen in the satellite and aircraft comparison. Instead, there must be errors in the NO_y production (i.e., NO_x emission rates are too low) or removal rates (i.e., NO_y deposition rates are too slow).

3.5 Comparison of OMI NO$_2$ to Pandora NO$_2$

To quantify the skill of the regional OMI NO_2 product, we compare the new total NO_2 vertical columns from the satellite product to the same quantities observed by the Pandora instruments. In Figure 6, monthly averaged observations during May 2016 from the Pandora instrument are overlaid onto the monthly average of the three OMI NO_2 satellite products. The two regional OMI NO_2 products capture the magnitude and spatial variability of monthly averaged NO_2 within the metropolitan region better.

We then compare daily Pandora observations to each daily OMI NO_2 value spatially and temporally co-located with the Pandora instrument (Figure 6). The Pandora observation is a 2-hour mean centered on the mid-afternoon OMI overpass. The slope of the linear best-fit of the standard product is 0.58, indicating that there is a consistent low bias in the satellite product when the Pandora instrument observes large values. The best-fit slope of the OMI-Regional product with only the air mass factor adjustment (AMF) is 0.76, and the OMI-Regional product with the air mass

factor adjustment and spatial kernel (AMF+SK) is 1.07, indicating that the regional products capture the polluted-to-clean spatial gradients best. The correlation of daily observations to the satellite retrievals does not improve between retrievals (OMI-Standard: $r^2 = 0.57$, OMI-Regional (AMF): $r^2 = 0.57$, and OMI-Regional (AMF+SK): $r^2 = 0.58$). The lack of improvement in the correlation suggests that the forecasted WRF-Chem simulation is unable to capture the daily variability of NO_2 plumes better than a longer-term average.

3.6 Estimating NO_x emissions from Seoul

To estimate NO_x emissions from the Seoul metropolitan area using a top-down satellite-based approach, we follow the exponentially modified Gaussian (EMG) fitting methodology outlined in Section 2.5. When fit using the EMG method, the photochemical lifetime and OMI NO_2 burden can be derived. Using this information, a NO_x emission rate can be inferred.

3.6.1. Validating the EMG method using WRF-Chem

The WRF-Chem simulation can serve as a test bed to assess the accuracy of the EMG method, since the bottom-up emissions used for the simulation are known. For this study, we find that for Seoul, an across plume width of 160 km encompasses the entire NO_2 downwind plume. Using the NO_2 lifetime, NO_2 burden, and a 160 km across plume width, we calculate the top-down NO_x emissions rate in the WRF-Chem simulation from the Seoul metropolitan area during the early afternoon (Figure 7). We find the effective NO_2 photochemical lifetime to be 3.1 ± 1.3 hours and the emissions rate to be 227 ± 94 kton/yr NO_2 equivalent. Uncertainties of the top-down NO_x emissions are the square root of the sum of the squares of: the NO_x / NO_2 ratio (10%), the OMI NO_2 vertical columns (25%), the across plume width (10%), and the wind fields (30%) (Lu et al., 2015). Only the latter three terms are used to calculate the uncertainty of the NO_2 lifetime (Lu et al., 2015).

The NO_x bottom-up emissions inventory calculated using a 40 km radius from the Seoul city center is 198 kton/yr NO_2 equivalent. We use a 40 km radius in lieu of a larger radius because an assumption in EMG method is that the emissions must be clustered around a single point (in this case, the city center). Therefore, the calculated emissions rate from the EMG fit is only measuring the magnitude of the perturbing emission source, and not of smaller sources that are further from the city center. Previous studies (de Foy et al., 2014; de Foy et al., 2015) suggest that the background level calculated by the EMG fit accounts for emissions outside the plume that are more regional and diffuse in nature. The agreement between the top-down (227 kton/yr) and bottom-up (198 kton/yr) approaches demonstrates the accuracy and effectiveness of the EMG method in estimating the emissions rate.

3.6.2. Deriving emissions using OMI NO_2

We now calculate the top-down NO_x emissions rate from the satellite data from the Seoul metropolitan area during the early afternoon (Figure 8). Here we use the OMI standard product and the OMI NO_2 retrieval without the spatial averaging kernel; only the new air mass factor is applied to this retrieval. We do not use the retrieval with the spatial averaging kernel when calculating top-down NO_x emissions because the spatial averaging is strongly dependent on

12

the wind fields in the WRF-Chem simulation, which are forecasted. Errors in the winds can greatly affect the estimate using this top-down approach (Valin et al., 2013; de Foy et al., 2014).

For the standard product, the effective NO_2 photochemical lifetime is 4.2 ± 1.7 hours, while in the regional product, the effective lifetime is 3.4 ± 1.4 hours. In the standard product, we derive the NO_x emissions rate to be 353 ± 146 kton/yr NO_2 equivalent, while in the regional product it is 484 ± 201 kton/yr NO_2 equivalent. Emission estimates using satellite products with coarse resolution air mass factors will yield top-down emission estimates that are lower than reality. In this case, the regional satellite product yields NO_x emission rates that are 37% higher; we would expect similar results from other metropolitan regions. The top-down approach for the model simulation yielded a NO_x emission rate of 227 kton/yr, while the top-down approach using the satellite data yielded a 484 kton/yr NO_x emission rate: a 53% underestimate in the emissions inventory.

It should be noted that the NO_2 photochemical lifetime derived here is a fundamentally different quantity than the NO_2 lifetime observed by in situ measurements (de Foy et al., 2014; Lu et al., 2015) or derived by model simulations (Lamsal et al., 2010). This is because the lifetime calculation is extremely sensitive to the accuracy of the wind direction (de Foy et al., 2014). Inaccuracies in the wind fields introduce noise that shorten the tail of the fit. As a result, NO_2 photochemical lifetimes derived here are considered "effective" photochemical lifetimes and are universally shorter than the tropospheric column NO_2 lifetimes derived by model simulations (Lamsal et al., 2010). NOx sources at the outer portions of urban areas will lead to an artificially longer NO_2 lifetime. This partially compensates for the bias introduced by the wind direction. The effective photochemical lifetime is also different from the NO_2 lifetime derived by in situ measurements of NO_2 at the surface or within the boundary layer. In the boundary layer, NO_2 is consumed faster yielding lifetimes that are shorter than the lifetimes based on tropospheric columns (Nunnermacker et al., 2007).

3.7. Model simulation with increased NO_x emissions

To test whether an increase in the NO_x emission rate is appropriate for the Seoul metropolitan area, we conduct a simulation with NO_x emissions in the Seoul metropolitan area – within a 40 km radius of the city center – increased by a factor of 2.13, and analyze the results for May 2016. The 2.13 increase is representative of the change suggested by the top-down method (OMI-Regional: 484 kton/yr vs. WRF-Chem original: 227 kton/yr). This simulation was performed slightly differently than the original simulation in that it was a continuous month-long simulation and the outer domain was nudged to the reanalysis.

When comparing the new model simulation to in situ observations from the UC-Berkeley NO_2 and NCAR NO_y instruments aboard the DC-8 aircraft, we find that NO_2 concentrations are a bit high, but NO_y concentrations are in good agreement with WRF-Chem in the boundary layer when spatially and temporally co-located in the immediate Seoul metropolitan area (Figure 9). When comparing the new WRF-Chem simulation to the OMI-Regional product for May 2016 (Figure 10), we find no significant biases in the Seoul metropolitan area. In the area within 40 km of

the Seoul city center, NO_2 columns are now only 11% smaller. The better agreement in NO_2 and NO_y from a combination of aircraft and satellite data suggests that an increase in NO_x emissions by a factor of 2.13 is appropriate.

Finally, we re-process the air mass factors for May 2016 using the newest WRF-Chem simulation. In Figure 11, we show the OMI-Standard product, the OMI-Regional product with no scaling of the a priori profiles from the original WRF-Chem simulation, the OMI-Regional product with scaling of the original a priori profiles, and the OMI-Regional product with a priori profiles from the new WRF-Chem simulation. While using the new a priori profiles increases the OMI NO_2 retrieval further by 8%, this change is much smaller than the 37% increase associated with switching models and model resolution (i.e., Standard vs. Regional product).

4. Conclusions and Discussion

In this work, we use a high-resolution (4×4 km^2) WRF-Chem model simulation to re-calculate satellite NO_2 air mass factors over South Korea. We also apply a spatial averaging kernel to better account for the sub-pixel variability that cannot be observed by OMI. The regional OMI NO_2 retrieval yields increased tropospheric columns in city centers and near large industrial areas. In the area within 40 km of the Seoul city center, OMI NO_2 values are 1.37 larger in the regional product. Areas near large industrial sources have OMI NO_2 values that are >2 times larger. The increase in remotely sensed tropospheric vertical column contents in the Seoul metropolitan area is in better agreement with the Pandora NO_2 spectrometer measurements acquired during the KORUS-AQ field campaign.

Using the regional OMI NO_2 product with only the air mass factor correction applied, we derive the NO_x emissions rate from the Seoul metropolitan area to be 484 ± 201 kton/yr, while the standard NASA OMI NO_2 product gives an emissions rate of 353 ± 146 kton/yr. The WRF-Chem simulation yields a mid-afternoon NO_x emission rate of 227 ± 94 kton/yr. This suggests an underestimate in the bottom-up NO_x emissions from Seoul metropolitan area by 53%, when compared to the 484 kton/yr emissions rate from our top-down method. When comparing observed OMI NO_2 to the WRF-Chem model simulation, we find similar underestimates of NO_2 in the Seoul metropolitan area. The effective photochemical lifetime derived in the Seoul plume is 4.2 ± 1.7 hours using the standard OMI NO_2 product and 3.4 ± 1.4 hours using the regional product. The regional product yields shorter NO_2 lifetimes, although it is not a statistically significant difference. Finally, we show that a WRF-Chem simulation with an increase in the NO_x emissions by a factor of 2.13 yields a better comparison with aircraft observations of NO_2 and NO_y, and is in better agreement with the OMI-Regional NO_2 product developed herein.

It should be noted that the Seoul metropolitan area has complex geographical features, which adds further uncertainty to this analysis. The area has large topographical changes over short distances, including many hills (> 500 m) within the metropolitan area. Furthermore, the city is in close proximity to the Yellow Sea, which causes the area to be affected by sea breeze fronts, especially in the springtime, which is our period of focus. The localized mountain and sea breezes may not be fully captured by our 4×4 km^2 WRF-Chem simulation used to derive the OMI-Regional product or the ERA-interim dataset used to calculate top-down NO_x emissions. The effects of these features on local air quality have been documented elsewhere in the literature (Kim and Ghim, 2002; Lee et al., 2008; Ryu et al., 2013).

We do not expect any consistent bias to result from this added uncertainty. Nevertheless, the 4×4 km^2 simulation will capture topography and mesoscale phenomena better than a coarse global model and further supports the benefits of WRF-Chem over a global model to derive NO$_2$ vertical column contents.

We hypothesize that the temporalization of NO$_x$ emissions in the bottom-up emission inventory is a large remaining uncertainty. The satellite-derived emission rates are instantaneous rates at the time of the OMI overpass (~13:45 local time). This is a different quantity than a bottom-up NO$_x$ emission inventory, which is often a daily averaged or monthly averaged emission rate. For this study, we only attempt to derive a mid-afternoon NO$_x$ emission rate. Subsequently, we make sure to compare this to the mid-afternoon NO$_x$ emission rate from WRF-Chem. While bottom-up studies provide estimates of the diurnal variability of NO$_x$ emissions, these are very difficult to confirm from top-down approaches. Due to a consistent mid-afternoon overpass time, OMI or TROPOMI cannot address this issue. Due to boundary layer dynamics, this is also very difficult to constrain from ground-based and aircraft measurements. In the future, observations from a geostationary satellite instruments such as the Geostationary Environment Monitoring Spectrometer (GEMS) and Tropospheric Emissions: Monitoring Pollution (TEMPO), will be helpful in constraining the ratio of the mid-afternoon emissions rate to the 24-hour averaged emission rate.

Acknowledgments

References

Allen, D. J., Pickering, K. E., Pinder, R. W., Henderson, B. H., Appel, K. W., and Prados, A.: Impact of lightning-NO on eastern United States photochemistry during the summer of 2006 as determined using the CMAQ model, Atmos. Chem. Phys., 12, 1737-1758, 2012.

5 Beirle, S., Boersma, K. F., Platt, U., Lawrence, M. G., and Wagner, T.: Megacity Emissions and Lifetimes of Nitrogen Oxides Probed from Space, Science, 333, 1737-1739, 2011.

Boersma, K. F., Jacob, D. J., Bucsela, E. J., Perring, A. E., Dirksen, R., Yantosca, R. M., Park, R. J., Wenig, M. O., Bertram, T. H., and Cohen, R. C.: Validation of OMI tropospheric NO_2 observations during INTEX-B and application to constrain NOx emissions over the eastern United States and Mexico, Atmos. Environ., 42, 4480-
10 4497, 2008.

Boersma, K. F., Eskes, H. J., Dirksen, R. J., Veefkind, J. P., Stammes, P., Huijnen, V., Kleipool, Q. L., Sneep, M., Claas, J., and Leitão, J.: An improved tropospheric NO2 column retrieval algorithm for the Ozone Monitoring Instrument, Atmos. Meas. Tech., 4, 1905, 2011.

Boersma, K. F., Vinken, G. C. M., and Tournadre, J.: Ships going slow in reducing their NOx emissions: changes in
15 2005–2012 ship exhaust inferred from satellite measurements over Europe, Environ. Res. Lett., 10, 074007, 2015.

Bucsela, E., Krotkov, N., Celarier, E., Lamsal, L., Swartz, W., Bhartia, P., Boersma, K., Veefkind, J., Gleason, J., and Pickering, K.: A new algorithm for retrieving vertical column NO2 from nadir-viewing satellite instruments: applications to OMI, Atmos. Meas. Tech, 6, 1361-1407, 2013.

Burrows, J. P., Weber, M., Buchwitz, M., Rozanov, V., Ladstatter- ¨ Weißenmayer, A., Richter, A., DeBeek, R.,
20 Hoogen, R., Bramstedt, K., Eichmann, K.-U., Eisinger, M., and Perner, D.: The Global Ozone Monitoring Experiment (GOME): Mission Concept and First Scientific Results, J. Atmos. Sci., 56, 151–175, 1999.

Canty, T. P., Hembeck, L., Vinciguerra, T. P., Anderson, D. C., Goldberg, D. L., Carpenter, S. F., Allen, D. J., Loughner, C. P., Salawitch, R. J., and Dickerson, R. R.: Ozone and NOx chemistry in the eastern US: evaluation of CMAQ/CB05 with satellite (OMI) data, Atmos. Chem. Phys., 15, 10965-10982, 2015.

25 Chen, D., Zhou, B., Beirle, S., Chen, L. M., and Wagner, T.: Tropospheric NO_2 column densities deduced from zenith-sky DOAS measurements in Shanghai, China, and their application to satellite validation, Atmos. Chem. Phys., 9, 3641-3662, 2009.

Curier, R. L., Kranenburg, R., Segers, A. J. S., Timmermans, R. M. A., and Schaap, M.: Synergistic use of OMI NO_2 tropospheric columns and LOTOS–EUROS to evaluate the NOx emission trends across Europe, Remote Sensing
30 of Environment, 149, 58-69, 2014.

Day, D. A., Wooldridge, P. J., Dillon, M. B., Thornton, J. A., and Cohen, R. C.: A thermal dissociation laser-induced fluorescence instrument for in situ detection of NO_2, peroxy nitrates, alkyl nitrates, and HNO_3, J. Geophys. Res. Atmos., 107, ARTN 4046, 2002.

Dee, D. P., Uppala, S. M., Simmons, A. J., Berrisford, P., Poli, P., Kobayashi, S., Andrae, U., Balmaseda, M. A.,
35 Balsamo, G., Bauer, P., Bechtold, P., Beljaars, A. C. M., van de Berg, L., Bidlot, J., Bormann, N., Delsol, C., Dragani, R., Fuentes, M., Geer, A. J., Haimberger, L., Healy, S. B., Hersbach, H., Hólm, E. V., Isaksen, L., Kållberg, P., Köhler, M., Matricardi, M., McNally, A. P., Monge-Sanz, B. M., Morcrette, J.-J., Park, B.-K., Peubey, C., de Rosnay, P., Tavolato, C., Thépaut, J.-N., and Vitart, F.: The ERA-Interim reanalysis: configuration and performance of the data assimilation system, Q. J. Roy. Meteorol. Soc., 137, 553– 597, doi:10.1002/qj.828,
40 2011.

de Foy, B., Lu, Z., and Streets, D. G.: Satellite NO_2 retrievals suggest China has exceeded its NOx reduction goals from the twelfth Five-Year Plan, Scientific Reports, 6, 2016.

de Foy, B., Lu, Z., Streets, D. G., Lamsal, L. N., and Duncan, B. N.: Estimates of power plant NOx emissions and lifetimes from OMI NO_2 satellite retrievals, Atmos. Environ., 116, 1-11, 2015.

45 de Foy, B., Wilkins, J. L., Lu, Z., Streets, D. G., Duncan, B. N.: Model evaluation of methods for estimating surface emissions and chemical lifetimes from satellite data. Atmos. Environ. 98, 66-77, 2014.

Dobber, M., Kleipoo, Q., Dirksen, E., Levelt, P., Jaross, G., Taylor, S., Kelly, T., Flynn, L., Leppelmeier, G., and Rozemeijer, N.: Validation of Ozone Monitoring Instrument level 1b data products, J. Geophys. Res. Atmos., 113, D15S06, 2008.

50 Duncan, B. N., Lamsal, L. N., Thompson, A. M., Yoshida, Y., Lu, Z., Streets, D. G., Hurwitz, M. M., and Pickering, K. E.: A space based, high resolution view of notable changes in urban NOx pollution around the world (2005–2014), J. Geophys. Res. Atmos., 121, 976-996, 2016.

Flynn, C. M., Pickering, K. E., Crawford, J. H., Lamsal, L., Krotkov, N., Herman, J., Weinheimer, A., Chen, G., Liu, X., and Szykman, J.: Relationship between column-density and surface mixing ratio: Statistical analysis of O_3

and NO$_2$ data from the July 2011 Maryland DISCOVER-AQ mission, Atmos. Environ., 92, 429-441, 2014.

Goldberg, D. L., Lamsal, L. N., Loughner, C. P., Swartz, W. H., Lu, Z., and Streets, D. G.: A high-resolution and observationally constrained OMI NO2 satellite retrieval, Atmos. Chem. Phys., 17, 11403-11421, https://doi.org/10.5194/acp-17-11403-2017, 2017.

Goldberg, D. L., Vinciguerra, T. P., Anderson, D. C., Hembeck, L., Canty, T. P., Ehrman, S. H., Martins, D. K., Stauffer, R. M., Thompson, A. M., Salawitch, R. J., and Dickerson R. R.: CAMx ozone source attribution in the eastern United States using guidance from observations during DISCOVER-AQ Maryland, Geophys. Res. Lett., 43, https://dx.doi.org/10.1002/2015GL067332, 2016.

Grell, G., Peckham, S. E., Schmitz, R., McKeen, S. A., Frost, G., Skamarock, W. C., and Eder, B.: Fully coupled "online" chemistry within the WRF model, Atmospheric Environment, 39, 6957-6975, 10.1016/j.atmosenv.2005.04.027, 2005.

Han, K. M., Lee, S., Chang, L. S., and Song, C. H.: A comparison study between CMAQ-simulated and OMI-retrieved NO$_2$ columns over East Asia for evaluation of NOx emission fluxes of INTEX-B, CAPSS, and REAS inventories, Atmos. Chem. Phys., 15, 1913-1938, 2015.

Herman, J., Cede, A., Spinei, E., Mount, G., Tzortziou, M., and Abuhassan, N.: NO$_2$ column amounts from ground-based Pandora and MFDOAS spectrometers using the direct-sun DOAS technique: Intercomparisons and application to OMI validation, J. Geophys. Res., 114, D13307, 2009.

Herman, J., Spinei, E., Fried, A., Kim, J., Kim, J., Kim, W., Cede, A., Abuhassan, N., and Segal-Rozenhaimer, M.: NO2 and HCHO measurements in Korea from 2012 to 2016 from Pandora spectrometer instruments compared with OMI retrievals and with aircraft measurements during the KORUS-AQ campaign, Atmos. Meas. Tech., 11, 4583-4603, https://doi.org/10.5194/amt-11-4583-2018, 2018

Hilboll, A., Richter, A., and Burrows, J. P.: Long-term changes of tropospheric NO$_2$ over megacities derived from multiple satellite instruments, Atmos. Chem. Phys., 13, 4145-4169, 2013.

Hodzic, A., and Jimenez, J. L.: Modeling anthropogenically controlled secondary organic aerosols in a megacity: a simplified framework for global and climate models, Geosci. Model Dev., 4, 901-917, 10.5194/gmd-4-901-2011, 2011.

Hudman, R. C., Russell, A. R., Valin, L. C., and Cohen, R. C.: Interannual variability in soil nitric oxide emissions over the United States as viewed from space, Atmos. Chem. Phys., 10, 9943-9952, 2010.

Huijnen, V., Eskes, H. J., Poupkou, A., Elbern, H., Boersma, K. F., Foret, G., Sofiev, M., Valdebenito, A., Flemming, J., Stein, O., Gross, A., Robertson, L., D'Isidoro, M., Kioutsioukis, I., Friese, E., Amstrup, B., Bergstrom, R., Strunk, A., Vira, J., Zyryanov, D., Maurizi, A., Melas, D., Peuch, V.-H., and Zerefos, C.: Comparison of OMI NO$_2$ tropospheric columns with an ensemble of global and European regional air quality models, Atmos. Chem. Phys., 10, 3273-3296, doi:10.5194/acp-10-3273-2010, 2010.

Ialongo, I., Herman, J., Krotkov, N., Lamsal, L., Boersma, K. F., Hovila, J., and Tamminen, J.: Comparison of OMI NO$_2$ observations and their seasonal and weekly cycles with ground-based measurements in Helsinki, Atmos. Meas. Tech., 9, 5203, 2016.

Inness, A., Blechschmidt, A. M., Bouarar, I., Chabrillat, S., Crepulja, M., Engelen, R. J., Eskes, H., Flemming, J., Gaudel, A., Hendrick, F., Huijnen, V., Jones, L., Kapsomenakis, J., Katragkou, E., Keppens, A., Langerock, B., de Mazière, M., Melas, D., Parrington, M., Peuch, V. H., Razinger, M., Richter, A., Schultz, M. G., Suttie, M., Thouret, V., Vrekoussis, M., Wagner, A., and Zerefos, C.: Data assimilation of satellite retrieved ozone, carbon monoxide and nitrogen dioxide with ECMWF's Composition-IFS, Atmos. Chem. Phys. Discuss., 15, 4265-4331, 10.5194/acpd-15-4265-2015, 2015.

Kim, H. C., Lee, P., Judd, L., Pan, L., and Lefer, B.: OMI NO$_2$ column densities over North American urban cities: the effect of satellite footprint resolution, Geosci. Mod. Dev., 9, 1111-1123, 2016.

Kim, J. Y., and Ghim, Y. S.: Effects of the density of meteorological observations on the diagnostic wind fields and performance of photochemical modeling in the great Seoul area, Atmos. Environ., 36, 201-212, 2002.

Kleipool, Q. L., Dobber, M. R., de Haan, J. F., and Levelt, P. F.: Earth surface reflectance climatology from 3 years of OMI data, J. Geophys. Res, Atmos,, 113, 2008.

Krotkov, N. A., McLinden, C. A., Li, C., Lamsal, L. N., Celarier, E. A., Marchenko, S. V., Swartz, W. H., Bucsela, E. J., Joiner, J., and Duncan, B. N.: Aura OMI observations of regional SO$_2$ and NO$_2$ pollution changes from 2005 to 2014, Atmos. Chem. Phys., 16, 4605-4629, 2016.

Krotkov, N. A., Lamsal, L. N., Celarier, E. A., Swartz, W. H., Marchenko, S. V., Bucsela, E. J., Chan, K. L., and Wenig, M. O.: The version 3 OMI NO$_2$ standard product, Atmos. Meas. Tech. Discuss., in review, 2017.

Kuhlmann, G., Lam, Y. F., Cheung, H. M., Hartl, A., Fung, J. C. H., Chan, P. W., and Wenig, W. O.: Development of a custom OMI NO$_2$ data product for evaluating biases in a regional chemistry transport model, Atmos. Chem. Phys., 15, 5627-5644, 2015.

Lamsal, L. N., Martin, R. V., van Donkelaar, A., Steinbacher, M., Celarier, E. A., Bucsela, E., Dunlea, E. J., and Pinto, J. P.: Ground-level nitrogen dioxide concentrations inferred from the satellite-borne Ozone Monitoring Instrument, J. Geophys. Res., 113, D16308, 2008.

Lamsal, L. N., Martin, R. V., van Donkelaar, A., Celarier, E. A., Bucsela, E. J., Boersma, K. F., Dirksen, R., Luo, C., and Wang, Y.: Indirect validation of tropospheric nitrogen dioxide retrieved from the OMI satellite instrument: Insight into the seasonal variation of nitrogen oxides at northern midlatitudes, J. Geophys. Res., 115, D05302, doi:10.1029/2009jd013351, 2010.

Lamsal, L. N., Krotkov, N. A., Celarier, E. A., Swartz, W. H., Pickering, K. E., Bucsela, E. J., Gleason, J. F., Martin, R. V., Philip, S., and Irie, H.: Evaluation of OMI operational standard NO_2 column retrievals using in situ and surface-based NO_2 observations, Atmos. Chem. Phys., 14, 11587-11609, 2014.

Lamsal, L. N., Duncan, B. N., Yoshida, Y., Krotkov, N. A., Pickering, K. E., Streets, D. G., and Lu, Z.: US NO_2 trends (2005 - 2013): EPA Air Quality System (AQS) data versus improved observations from the Ozone Monitoring Instrument (OMI), Atmos. Environ., 110, 130-143, 2015.

Laughner, J. L., Zare, A., and Cohen, R. C.: Effects of daily meteorology on the interpretation of space-based remote sensing of NO_2, Atmos. Chem. Phys., 16, 15247-15264, 2016.

Lee, H. W., Choi, H.-J., Lee, S.-H., Kim, Y.-K., Jung, W.-S.: The impact of topography and urban building parameterization on the photochemical ozone concentration of Seoul, Korea, Atmos. Environ., 42(18), 4232-4246, 2008.

Levelt, P. F., Van den Oord, G. H. J., Dobber, M. R., Malkki, A., Visser, H., de Vries, J., Stammes, P., Lundell, J. O. V., and Saari, H.: The Ozone Monitoring Instrument, IEEE Trans. Geosci. Rem. Sens., 44, 1093-1101, 2006.

Liaskos, C. E., Allen, D. J., and Pickering, K. E.: Sensitivity of tropical tropospheric composition to lightning NOx production as determined by replay simulations with GEOS-5, J. Geophys. Res. Atmos., 2015.

Lin, J. T., Liu, M. Y., Xin, J. Y., Boersma, K. F., Spurr, R., Martin, R., and Zhang, Q.: Influence of aerosols and surface reflectance on satellite NO_2 retrieval: seasonal and spatial characteristics and implications for NOx emission constraints, Atmos. Chem. Phys, 15, 11217-11241, 2015.

Liu, F., Beirle, S., Zhang, Q., Dörner, S., He, K., and Wagner, T.: NOx lifetimes and emissions of cities and power plants in polluted background estimated by satellite observations, Atmos. Chem. Phys., 16, 5283-5298, https://doi.org/10.5194/acp-16-5283-2016, 2016.

Liu, F., Beirle, S., Zhang, Q., van der A, R. J., Zheng, B., Tong, D., and He, K.: NOx emission trends over Chinese cities estimated from OMI observations during 2005 to 2015, Atmos. Chem. Phys., 17, 9261-9275, https://doi.org/10.5194/acp-17-9261-2017, 2017.

Lorente, A., Boersma, K. F., Yu, H., Dörner, S., Hilboll, A., Richter, A., Liu, M., Lamsal, L. N., Barkley, M., and De Smedt, I.: Structural uncertainty in air mass factor calculation for NO2 and HCHO satellite retrievals, Atmos. Meas. Tech., 10, 759, 2017.

Lu, Z., Streets, D. G., de Foy, B., Lamsal, L. N., Duncan, B. N., and Xing, J.: Emissions of nitrogen oxides from US urban areas: estimation from Ozone Monitoring Instrument retrievals for 2005–2014, Atmos. Chem. Phys., 15, 10367-10383, 2015.

Ma, J. Z., Beirle, S., Jin, J. L., Shaiganfar, R., Yan, P., and Wagner, T.: Tropospheric NO2 vertical column densities over Beijing: results of the first three years of ground-based MAX-DOAS measurements (2008–2011) and satellite validation, Atmos. Chem. Phys., 13, 1547-1567, 2013.

Martin, R. V., Chance, K., Jacob, D. J., Kurosu, T. P., Spurr, R. J. D., Bucsela, E., Gleason, J. F., Palmer, P. I., Bey, I., and Fiore, A. M.: An improved retrieval of tropospheric nitrogen dioxide from GOME, J. Geophys. Res. Atmos., 107, 2002.

Miyazaki, K., Eskes, H., Sudo, K., Boersma, K. F., Bowman, K., and Kanaya, Y.: Decadal changes in global surface NOx emissions from multi-constituent satellite data assimilation, Atmos. Chem. Phys., 17, 807-837, https://doi.org/10.5194/acp-17-807-2017, 2017.

Nault, B. A., Laughner, J. L., Wooldridge, P. J., Crounse, J. D., Dibb, J., Diskin, G., Peischl, J., Podolske, J. R., Pollack, I. B., Ryerson, T. B., Scheuer, E., Wennberg, P. O., and Cohen, R. C.: Lightning NOx Emissions: Reconciling Measured and Modeled Estimates With Updated NOx Chemistry, Geophys. Res. Lett., 44, 9479–9488, https://doi.org/10.1002/2017GL074436, 2017.

Palmer, P. I., Jacob, D. J., Chance, K. V., Martin, R. V., Spurr, R. J. D., Kurosu, T., Bey, I., Yantosca, R. M., Fiore, A., and Li, Q.: Air mass factor formulation for spectroscopic measurements from satellites: Application to formaldehyde retrievals from the Global Ozone Monitoring Experiment, J. Geophys. Res., 106, 14539-14550, 2001.

Pfister, G. G., Walters, S., Lamarque, J. F., Fast, J., Barth, M. C., Wong, J., Done, J., Holland, G., and Bruyère, C. L.: Projections of future summertime ozone over the U.S, Journal of Geophysical Research: Atmospheres, 119, 5559-

5582, 10.1002/2013jd020932, 2014.

Pickering, K. E., Bucsela, E., D, Ring, A., Holzworth, R., and Krotkov, N.: Estimates of lightning NOx production based on OMI NO_2 observations over the Gulf of Mexico, J. Geophys. Res. Atmos., 121, 8668-8691, 2016.

Platt, U.: Differential optical absorption spectroscopy (DOAS), Air monitoring by spectroscopic technique, 127, 27-84, 1994.

Pujadas, M., Núñez, L., and Lubrani, P.: Assessment of NO_2 satellite observations for en-route aircraft emissions detection, Remote Sensing of Environment, 115, 3298-3312, 2011.

Rasool, Q. Z., Zhang, R., Lash, B., and Cohan, D. S., Cooter, E. J., Bash, J. O., Lamsal, L. N.: Enhanced representation of soil NO emissions in the Community Multiscale Air Quality (CMAQ) model version 5.0. 2, Geosci. Mod. Dev., 9, 3177-3197, 2016.

Ridley, B., Ott, L., Pickering, K., Emmons, L., Montzka, D., Weinheimer, A., Knapp, D., Grahek, F., Li, L., Heymsfield, G., McGill, M., Kucera, P., Mahoney, M. J., Baumgarner, D., Schultz, M., and Brasseur, G..: Florida thunderstorms: A faucet of reactive nitrogen to the upper troposphere, J. Geophys. Res. Atmos., 109, D17305, 2004.

Romer, P. S., Duffey, K. C., Wooldridge, P. J., Allen, H. M., Ayres, B. R., Brown, S. S., Brune, W. H., Crounse, J. D., de Gouw, J., Draper, D. C., Feiner, P. A., Fry, J. L., Goldstein, A. H., Koss, A., Misztal, P. K., Nguyen, T. B., Olson, K., Teng, A. P., Wennberg, P. O., Wild, R. J., Zhang, L., and Cohen, R. C.: The lifetime of nitrogen oxides in an isoprene-dominated forest, Atmos. Chem. Phys., 16, 7623-7637, https://doi.org/10.5194/acp-16-7623-2016, 2016.

Russell, A. R., Valin, L. C., Bucsela, E. J., Wenig, M. O., and Cohen, R. C.: Space-based constraints on spatial and temporal patterns of NO_x emissions in California, 2005-2008, Environ. Sci. Technol., 44, 3608-3615, 2010.

Russell, A. R., Perring, A. E., Valin, L. C., Bucsela, E. J., Browne, E. C., Wooldridge, P. J., and Cohen, R. C.: A high spatial resolution retrieval of NO_2 column densities from OMI: method and evaluation, Atmos. Chem. Phys., 11, 8543-8554, 2011.

Ryu, Y.-H., Baik, J.-J., Kwak, K.-H., Kim, S., and Moon, N.: Impacts of urban land-surface forcing on ozone air quality in the Seoul metropolitan area, Atmos. Chem. Phys., 13, 2177-2194, https://doi.org/10.5194/acp-13-2177-2013, 2013.

Saide, P. E., Carmichael, G. R., Liu, Z., Schwartz, C. S., Lin, H. C., da Silva, A. M., and Hyer, E.: Aerosol optical depth assimilation for a size-resolved sectional model: impacts of observationally constrained, multi-wavelength and fine mode retrievals on regional scale forecasts, Atmos. Chem. Phys. Discuss., 13, 12213-12261, 10.5194/acpd-13-12213-2013, 2013.

Saide, P. E., Kim, J., Song, C. H., Choi, M., Cheng, Y., and Carmichael, G. R.: Assimilation of next generation geostationary aerosol optical depth retrievals to improve air quality simulations, Geophysical research letters, 41, 2014GL062089, 10.1002/2014gl062089, 2014.

Skamarock, W. C., Klemp, J. B., Dudhia, J., Gill, D. O., Barker, D. M., Duda, M. G., Huang, X.-Y., Wang, W., and Powers, J. G.: A description of the Advanced Research WRF version 3, NCAR Tech. Note NCAR/TN-475+ STR, 2008.

Souri, A. H., Choi, Y., Jeon, W., Li, X., Pan, S., Diao, L., and Westenbarger, D. A.: Constraining NOx emissions using satellite NO_2 measurements during 2013 DISCOVER-AQ Texas campaign, Atmos. Environ., 131, 371-381, 2016.

Souri, A. H., Choi, Y., Jeon, W., Woo, J., Zhang, Q., and Kurokawa, J.: Remote sensing evidence of decadal changes in major tropospheric ozone precursors over East Asia J. Geophys. Res, Atmos., 2017.

Streets, D. G., Canty, T., Carmichael, G. R., de Foy, B., Dickerson, R. R., Duncan, B. N., Edwards, D. P., Haynes, J. A., Henze, D. K., Houyoux, M. R., Jacob, D. J., Krotkov, N. A., Lamsal, L. N., Liu, Y., Lu, Z., Martin, R. V., Pfister, G. G., Pinder R. W., Salawitch, R. J., Wecht, K. J.: Emissions estimation from satellite retrievals: A review of current capability, Atmos. Environ., 77, 1011-1042, 2013.

Thornton, J. A., Wooldridge, P. J., and Cohen R. C.: Atmospheric NO_2: In situ laser-induced fluorescence detection at parts per trillion mixing ratios, Analytical Chemistry, 72, 528-539, 2000.

Valin, L. C., Russell, A. R., and Cohen, R. C.: Variations of OH radicals in an urban plume inferred from NO_2 column measurements. Geophys. Res. Lett., 40, 1856-1860, 2013.

van der A, R. J., Mijling, B., Ding, J., Koukouli, M. E., Liu, F., Li, Q., Mao, H., Theys, N.: Cleaning up the air: effectiveness of air quality policy for SO_2 and NO_x emissions in China, Atmos. Chem. Phys., 17, 1775–1789, 2017.

van Vuuren, D. P., Bouwman, L. F., Smith, S. J., and Dentener, F.: Global projections for anthropogenic reactive nitrogen emissions to the atmosphere: an assessment of scenarios in the scientific literature, Current Opinion in

20

Environmental Sustainability, 3, 359-369, 2011.

Vandaele, A. C., Hermans, C., Simon, P. C., Carleer, M., Colin, R., Fally, S., Merienne, M.-F., Jenouvrier, A., and Coquart, B.: Measurements of the NO_2 absorption cross-section from 42 000 cm− 1 to 10 000 cm− 1 (238–1000 nm) at 220 K and 294 K, Journal of Quantitative Spectroscopy and Radiative Transfer, 59, 171-184, 1998.

Vasilkov, A., Qin, W., Krotkov, N., Lamsal, L., Spurr, R., Haffner, D., Joiner, J., Yang, E.-S., and Marchenko, S.: Accounting for the effects of surface BRDF on satellite cloud and trace-gas retrievals: a new approach based on geometry-dependent Lambertian equivalent reflectivity applied to OMI algorithms, Atmos. Meas. Tech., 10, 333-349, https://doi.org/10.5194/amt-10-333-2017, 2017.

Vinken, G. C. M., Boersma, K. F., Maasakkers, J. D., Adon, M., and Martin, R. V.: Worldwide biogenic soil NOx emissions inferred from OMI NO_2 observations, Atmos. Chem. Phys., 14, 10363-10381, 2014a.

Vinken, G. C. M., Boersma, K. F., van Donkelaar, A., and Zhang, L.: Constraints on ship NOx emissions in Europe using GEOS-Chem and OMI satellite NO2 observations, Atmos. Chem. Phys., 14, 1353-1369, 2014b.

Woo, J. H., Choi, K. C., Kim, H. K., Baek, B. H., Jang, M., Eum, J. H., Song, C. H., Ma, Y. I., Sunwoo, Y., Chang, L. S., and Yoo, S. H.: Development of an anthropogenic emissions processing system for Asia using SMOKE, Atmos. Environ., 58, 5–13, 2012.

Zaveri, R. A., Easter, R. C., Fast, J. D., and Peters, L. K.: Model for simulating aerosol interactions and chemistry (MOSAIC), J. Geophys. Res, 113, D13204, 2008.

Zhang, L., Jacob, D. J., Boersma, K. F., Jaffe, D. A., Olson, J. R., Bowman, K. W., Worden, J. R., Thompson, A. M., Avery, M. A., Cohen, R. C., Dibb, J. E., Flock, F. M., Fuelberg, H. E., Huey, L. G., McMillan, W. W., Singh, H. B., and Weinheimer, A. J.: Transpacific transport of ozone pollution and the effect of recent Asian emission increases on air quality in North America: an integrated analysis using satellite, aircraft, ozonesonde, and surface observations, Atmos. Chem. Phys., 8, 6117-6136, 2008.

Zheng, B., Tong, D., Li, M., Liu, F., Hong, C., Geng, G., Li, H., Li, X., Peng, L., Qi, J., Yan, L., Zhang, Y., Zhao, H., Zheng, Y., He, K., and Zhang, Q.: Trends in China's anthropogenic emissions since 2010 as the consequence of clean air actions, Atmos. Chem. Phys., 18, 14095-14111, https://doi.org/10.5194/acp-18-14095-2018, 2018.

Zhou, Y., Brunner, D., Spurr, R. J. D., Boersma, K. F., Sneep, M., Popp, C., and Buchmann, B.: Accounting for surface reflectance anisotropy in satellite retrievals of tropospheric NO2, Atmos. Meas. Tech., 3, 1185-1203, https://doi.org/10.5194/amt-3-1185-2010, 2010.

Zhou, Y., Brunner, D., Boersma, K. F., Dirksen, R., and Wang, P.: An improved tropospheric NO2 retrieval for OMI observations in the vicinity of mountainous terrain, Atmos. Meas. Tech., 2, 401-416, https://doi.org/10.5194/amt-2-401-2009, 2009.
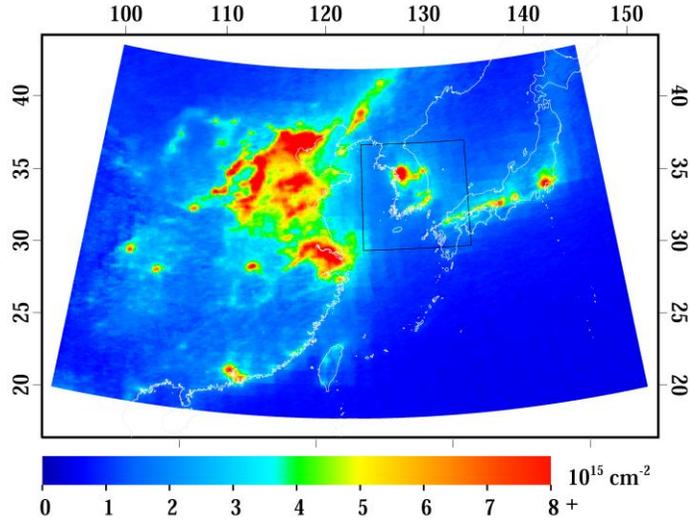
Figure 1. Warm season averaged (May – Sept) NO$_2$ tropospheric vertical column content using the OMI-Standard NO$_2$ product for the years of 2015 – 2017 in East Asia. The 4×4 km^2 WRF-Chem domain is outlined over the Korean peninsula.

5
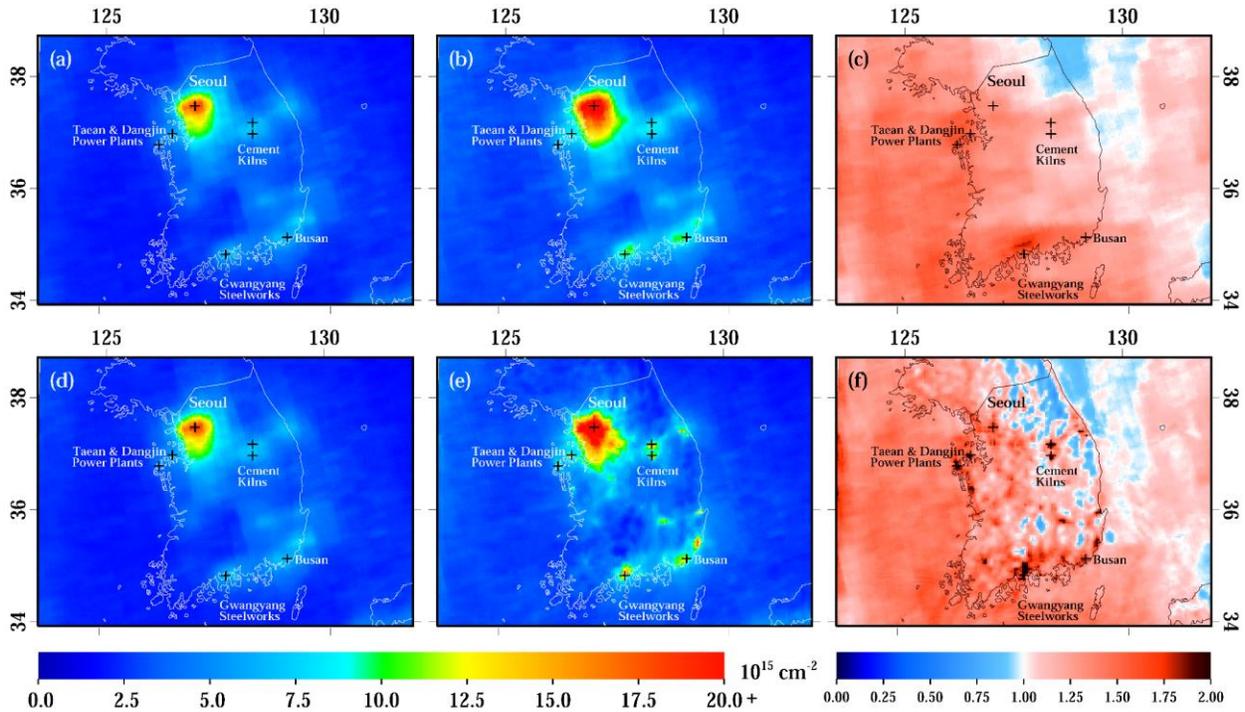
Figure 2. (a) OMI-Standard NO$_2$ product averaged over a 9-month period, Apr – Jun 2015 – 2017, (b) the OMI-Regional NO$_2$ product with only the air mass factor adjustment averaged over the same timeframe, and (c) the ratio between the two products. (d) Same as the top left plot, (e) the OMI-Regional NO$_2$ product with the air mass factor adjustment and spatial kernel averaged over the same timeframe, and (f) the ratio between the two products.

10

20
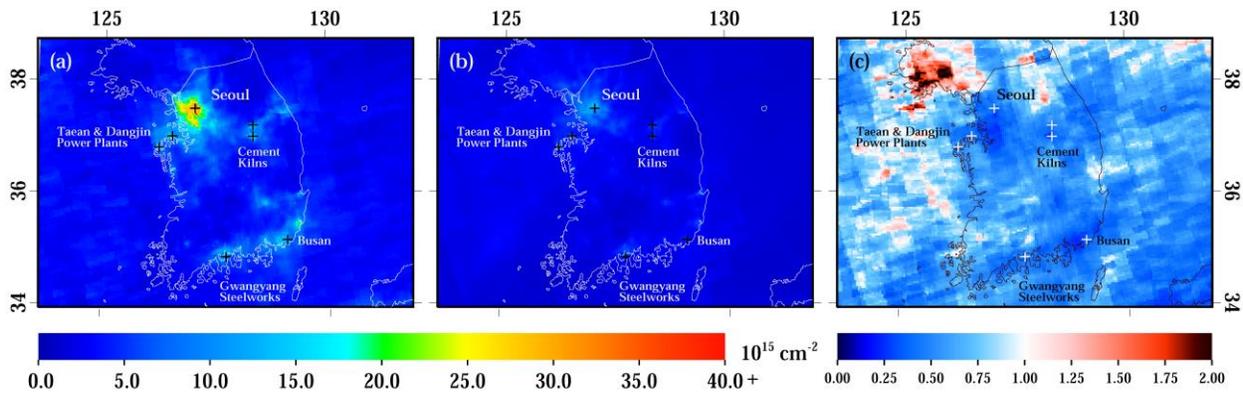
Figure 3. (a) The OMI-Regional NO$_2$ product with the air mass factor adjustment and spatial kernel averaged during the month of May 2016, (b) the WRF-Chem model simulation showing only days with valid OMI measurements, and (c) the ratio between the two products. On average, there are only 9 valid OMI pixels per month observed at any given location on the Korean peninsula during May 2016.
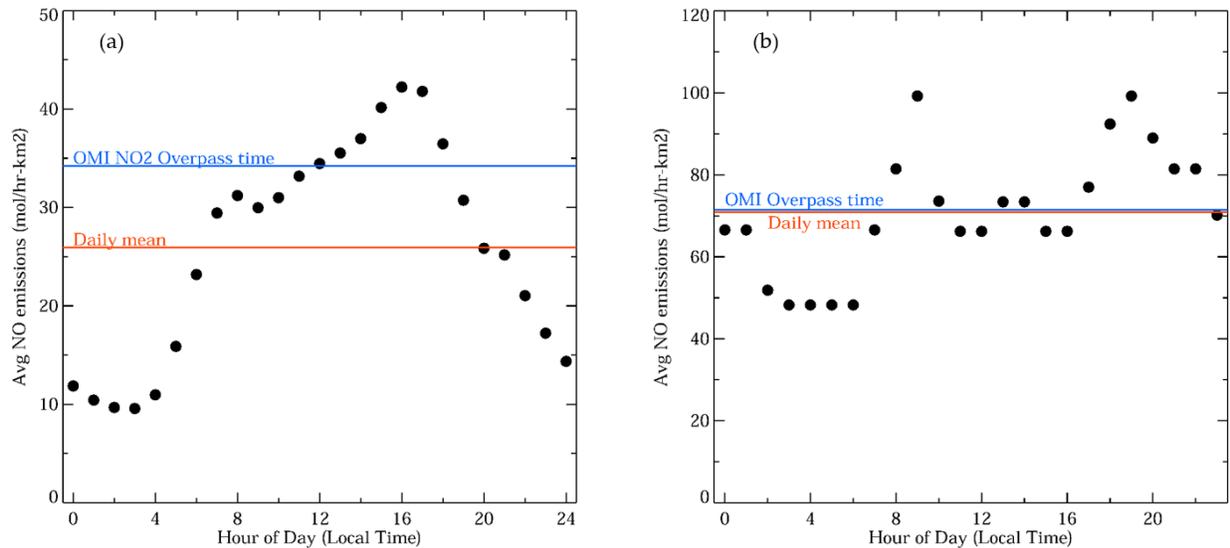

Figure 4. The diurnal profile of NO$_x$ emission rates processed from the bottom-up inventory. (a) The diurnal profile of NO$_x$ emission rates during a weekday in the eastern USA during July 2011 using SMOKE as the emissions pre-processor (Goldberg et al., 2016). (b) The diurnal profile of emission rates during a weekday in Korea during May 2016 using EPRES as the emissions pre-processor. Emission profiles in the right panel were used in the WRF-Chem simulation.

21
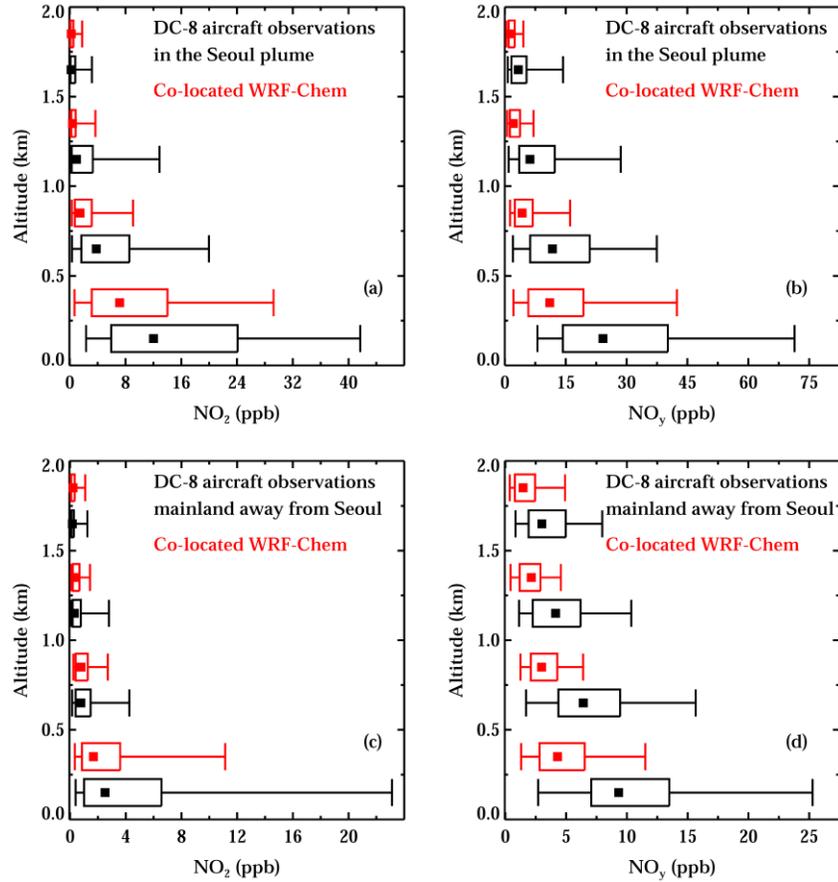
Figure 5. Measurements from the DC-8 aircraft binned by altitude in black. Co-located WRF-Chem within the same altitude bin as the aircraft observations are plotted above in red. Square dots represent the median values. Boxes represent the 25th and 75th percentiles, while whiskers represent the 5th and 95th percentiles. (a) Comparison of NO_2 in the Seoul plume (SW corner: 37.1° N, 127.05° E, NE corner: 37.75° N, 127.85° E) (b) comparison of NO_y in the Seoul plume, (c) comparison of NO_2 in areas outside of the Seoul metropolitan area on the Korean peninsula (SW corner: 34.0° N, 126.4° E, NE corner: 37.1° N, 130.0° E), and (d) comparison of NO_y in areas outside of the Seoul metropolitan area on the Korean peninsula.

22
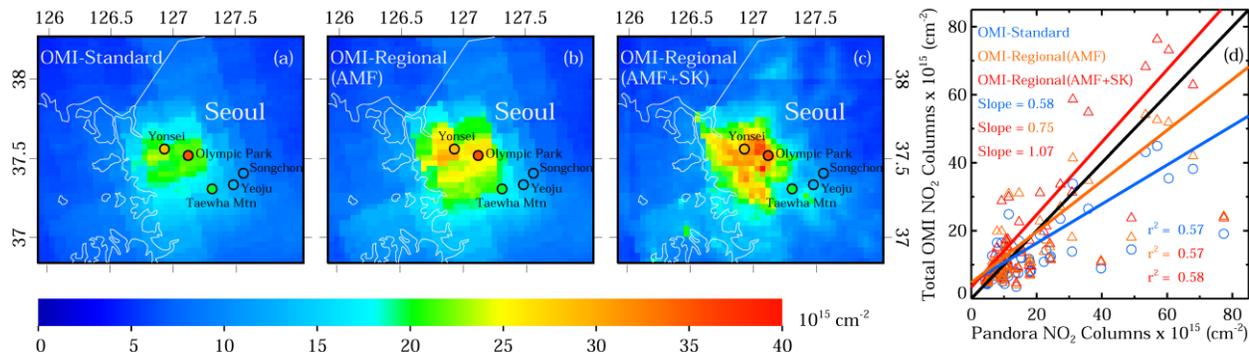
Figure 6. (a) Total vertical column contents from the OMI-Standard NO$_2$ product for May 2016, (b) same quantities from the OMI-Regional product with only the air mass factor adjustment (AMF) during the same timeframe, (c) same quantities from the OMI-Regional product with the air mass factor adjustment and spatial kernel (AMF+SK) during the same timeframe, and (d) a comparison between total column contents from the three OMI NO$_2$ products and Pandora NO$_2$ during May 2016. An average of Pandora 2-hour means co-located to valid daily OMI overpasses are overlaid in the spatial plots.
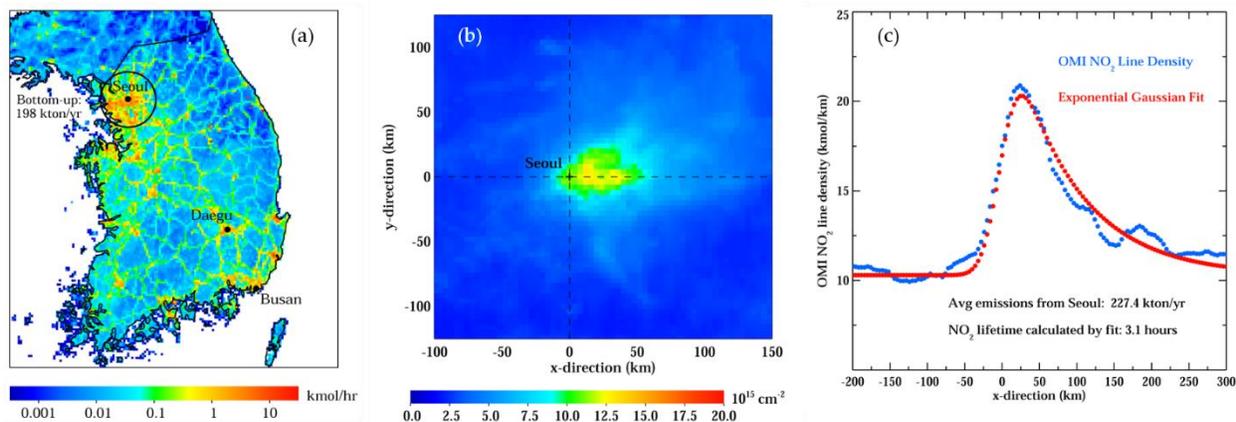
Figure 7. (a) Bottom-up NO$_x$ emissions inventory compiled for the KORUS-AQ field campaign, (b) the oversampled NO$_2$ plume rotated based on wind direction for Seoul, Korea from WRF-Chem (4 × 4 km^2) for May 2016, and (c) NO$_2$ line densities integrating over the 240 km across plume width (-120 km to 120 km along the y-axis) and the corresponding EMG fit. NO$_x$ emission estimates are shown in units of kton/yr NO$_2$ equivalent and represent the mid-afternoon emissions rate.

23
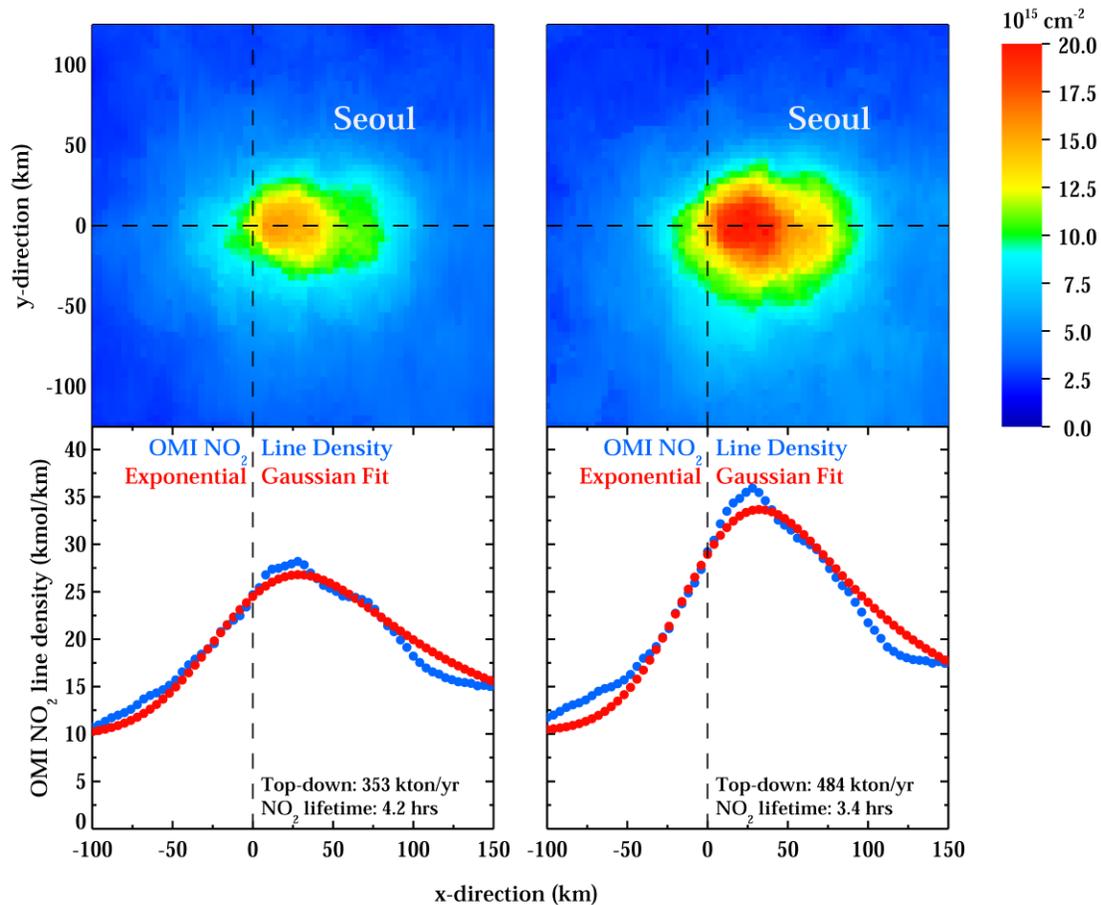
Figure 8. Top panels represent the oversampled (4 × 4 km²) OMI NO₂ plume from Seoul rotated based on wind direction over a 9-month period, Apr – Jun 2015 – 2017, centered on May 2016. Bottom panels represent the OMI NO₂ line densities integrating over the 240 km across plume width (-120 km to 120 km along the y-axis of the top panels) and the corresponding EMG fit. Left panels are from the OMI-Standard NO₂ product and right panels are from the OMI-Regional NO₂ product. NOₓ emission estimates are shown in units of kton/yr NO₂ equivalent and represent the mid-afternoon emissions rate.
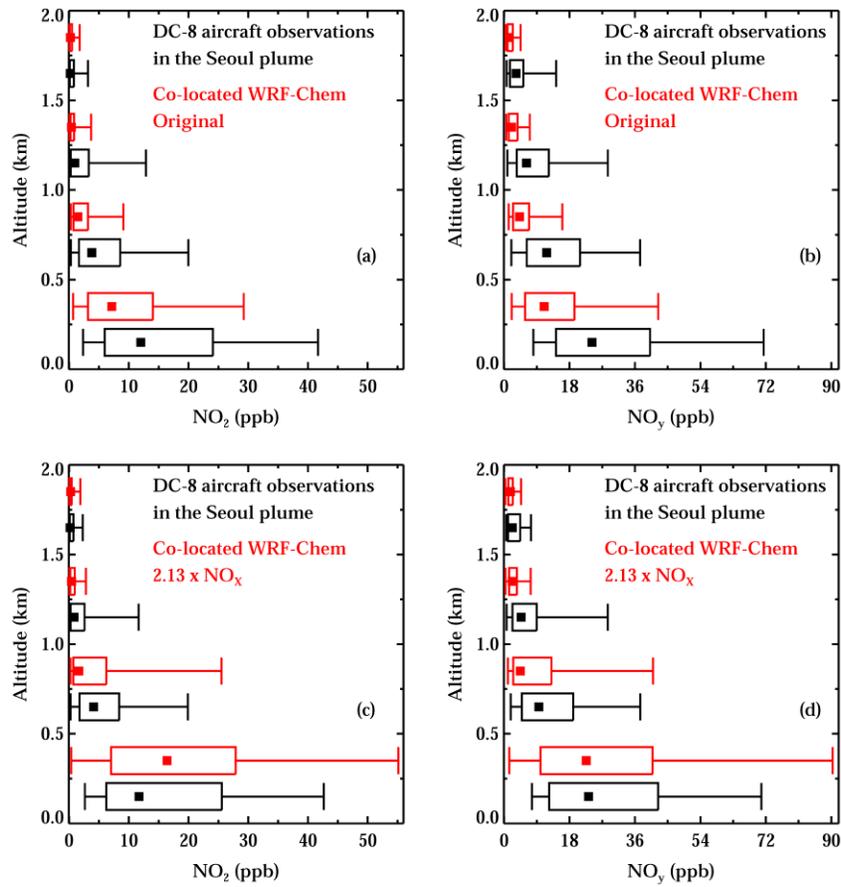
Figure 9. Measurements from the DC-8 aircraft binned by altitude in black. Co-located WRF-Chem within the same altitude bin as the aircraft observations are plotted above in red. Square dots represent the median values. Boxes represent the 25th and 75th percentiles, while whiskers represent the 5th and 95th percentiles. (a) Comparison of NO_2 in the Seoul plume (SW corner: 37.1° N, 127.05° E, NE corner: 37.75° N, 127.85° E) (b) comparison of NO_y in the Seoul plume, (c) same as (a), but now using the WRF-Chem simulation with NO_x emissions increased by a factor of 2.13 (d) same as (b), but now using the WRF-Chem simulation with NO_x emissions increased by a factor of 2.13.
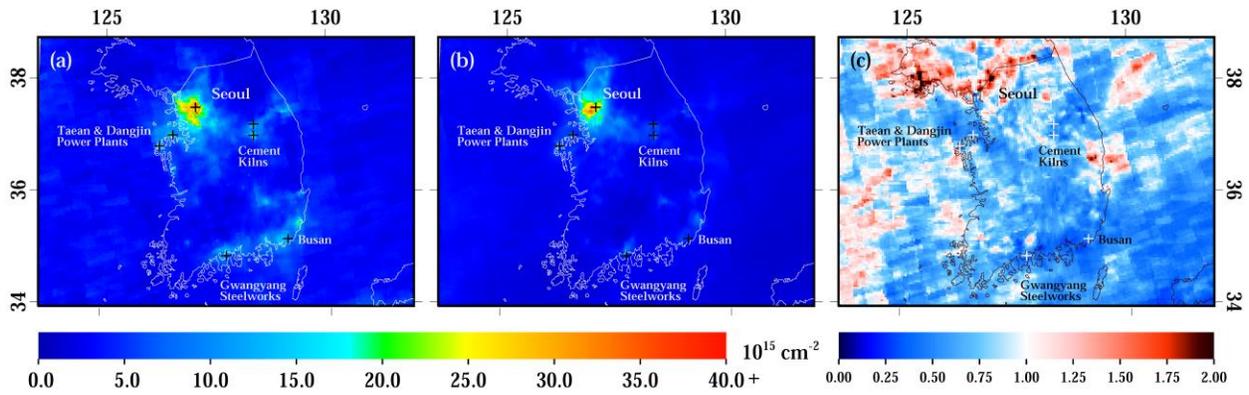
Figure 10. Same as Figure 3, but now showing the WRF-Chem simulation with NO_x emissions in the Seoul metropolitan area increased by a factor of 2.13 in panel (b).
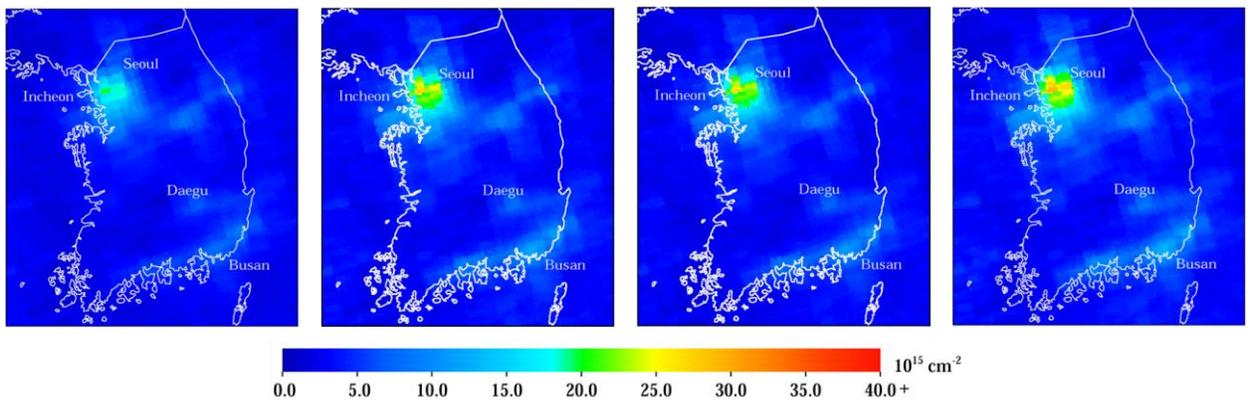

Figure 11. (a) The OMI-Standard product during the month of May 2016, (b) the OMI-Regional NO_2 product with the WRF-Chem air mass factor adjustment and spatial kernel during the same period, (c) same as (b) but using WRF-Chem NO_2 profiles scaled based on the aircraft comparison, and (d) same as (b) but using the WRF-Chem simulation with NO_x in the Seoul metropolitan area emissions increased by a factor of 2.13.